Microstructure effects on the local order and electronic defects in (Al, Ti, Mg) co-doped ZnO conductive ceramics

Qianying Sun, Guorong Li, Zhenyong Man, Liaoying Zheng, Malgorzata Makowska-Janusik, Maud Barré, Jens Dittmer, Sandy Auguste, Anthony Rousseau, Abdel Hadi Kassiba

Microstructure effects on the local order and electronic defects in (Al, Ti, Mg) co-doped ZnO conductive ceramics

Qianying Sun[a,b,c], Guorong Li[a,c], Zhenyong Man[a,c], Liaoying Zheng[a,c*], Malgorzata Makowska-Janusik[d], Maud Barré[b], Jens Dittmer[b], Sandy Auguste[b], Anthony Rousseau[b], and Abdel Hadi Kassiba[b*]

[a] Key Laboratory of Inorganic Functional Material and Device, Shanghai Institute of Ceramics, Chinese Academy of Sciences, 1295 Dingxi Road, Shanghai 200050, China

[b] Institute of Molecules and Materials of Le Mans (IMMM) – UMR - CNRS 6283, Le Mans Université, 72085 Le Mans Cedex 9, France

[c] Center of Materials Science and Optoelectronics Engineering, University of Chinese Academy of Sciences, Beijing 100049, China

[d] Institute of Physics, Faculty of Mathematics and Natural Science, Jan Dlugosz University in Czestochowa, Al. Armii Krajowej 13/15, 42200 Czestochowa, Poland

Abstract

Fine particles with different sizes of (Al, Ti, Mg) oxide co-doped ZnO ceramics were realized by a suitable grinding and a mechanical ball milling, respectively. The investigations were devoted to understand the origin of the electrical conductivity evolution with the microstructure by analyzing the local order and defect involvement in the crystalline sites of ZnO ceramics. Experimental investigations of particles were conducted to probe the local order and electronic defects with an emphasis on the electrical behavior of ceramics. Particularly, Al doping is intimately correlated with the high conductivity induced from the stabilization of particular Al_{Zn}-Zn_i complexes. The conduction electrons are probed through the induced Knight Shift on NMR spectra and also from the particular relaxation mechanisms of paramagnetic centers revealed by EPR studies. The correlation between the electronic active defects, the microstructure in small sized particles of ZnO based ceramics and the electrical behavior are pointed out and discussed.

Keywords: ZnO; Al doping; local order; electronic defects; particle size; conductivity;

magnetic resonance

*: Corresponding authors A. Kassiba (kassiba@univ-lemans.fr), L. Zheng (zhengly@mail.sic.ac.cn)

Introduction

ZnO belongs to the third generation of wide-band gap semiconductors with attractive properties such as a good transparency in the visible range, a high electron mobility, a large exciton binding energy and strong room temperature luminescence [1,2]. The high electrical conductive ZnO material is of a great interest in applications such as lithium-Ion batteries [3], solar cells [4], high-power gyrotrons [5], varistors [6], gas sensors [7], thermoelectric and photoelectric devices [8,9], etc. Donor doping is the common way to increase the electrical conductivity of ZnO as this material exhibits an intrinsic n-type behavior. The doping with group III elements such as (X= B, Al, Ga, In) is suitable approach to increase the carrier concentration and electron mobility in doped ZnO based compounds [8,10-12]. Among them, Al^{3+} are the most commonly used ions due to their non-toxicity, high abundance, environmentally friendly and low cost.

Recently, Momot et al. [13] suggested that Al_{Zn}-Zn_i complexes are relevant shallow donors for the high conductivity of Al-doped ZnO materials through Raman, nuclear magnetic resonance (NMR) and conductivity measurements combined with first-principles calculations in Al:ZnO nanoparticles. In the reported work, the Al atoms at interstitial positions migrate to the substitutional positions of Zn, creating Zn interstitials simultaneously and forming the complexes of Al_{Zn} and Zn_i, which increase the number of charge carriers. In our previous work [14,15], ZnO ceramics doped with Al_2O_3, TiO_2 and MgO have been realized by using suitable co-doping ratios along with different sintering atmospheres. A high conductivity up to 1.52×10^5 $S\cdot m^{-1}$ was obtained under the reducing atmosphere ($CO+N_2$). Al ions constitute the key doping elements to produce shallow donors as Al_{Zn}-Zn_i complexes. This leads to a huge

Knight Shifted effect on the ^{27}Al NMR through an extended charge delocalization to achieve that high conductivity of ZnO ceramics [15,16]. However, the NMR signal related to tetrahedral Al at the chemical shift of 80 ppm in ZnO:Al nanoparticles from Momot's work is quite intense than the same NMR peak from our ZnO ceramics. Thus we expect different distributions of defects between Al doped ZnO bulk ceramics compare to their counterpart nanoparticles. Thus, the main objective of the present work deals with the correlation between the microstructures of the bulk ceramics and samples with small sized particles by using resonance methods such NMR and EPR which probe the local structure of electronic active defects. Therefore, ZnO based ceramics were crushed to particles with different sizes from about 100 microns down to 0.2 microns scaled by using manual grinding or mechanically by ball milling process. The manually ground sample with large scale grains reflects the properties of bulk ceramics, while the ball milling sample leads to small sized ZnO particles with relevant effects from the surface. Thus, the relation between the defects structure and the electrical conductivity will be clarified by investigating the evolution of the environment of Al ions in the host ZnO lattice as function of the particle sizes. The approach is thought to ensure consistent understanding of the correlation between the defect structures, the microstructures and the electrical conductivity in the underlying ZnO based samples.

Experimental details

ZnO based ceramics were synthesized according to the molar ratios as 92.25 mol.% ZnO + 0.25 mol.% Al_2O_3 + 0.50 mol.% TiO_2 + 1.00 mol% MgO. The purity and the manufacturers of raw materials are indicated in Table 1. The ceramic fabrication was realized by the conventional solid state reaction method with the protocol hereafter outlined. The raw materials were weighed according to the designed ratios, and then uniformly mixed by a 6-hour ball milling. The mixed powder was granulated by adding PVA (polyvinyl alcohol) binder and then pressed into small pellets. After removing PVA binder

by annealing at 500 °C for 5 hours, all pellets were sintered at 1200 °C for 2 hours under N_2 + CO, which was realized by N_2 gas flow on dense media from pure carbon located in the close vicinity of the samples. The obtained ceramic pellets have the dimensions of 12 mm diameter and 1mm thickness; they are referred below as '**C**' samples and represent the bulk ceramics. To compare the features of **C** sample with their finely divided counterpart as particles with different sizes, the manual grinding and the ball milling were performed. Microscale particles in the range 10 μm-100 μm were obtained by the manual grinding, referred below as '**M**' samples, and the smaller size particles about 0.2 μm, referred as '**B**' samples were obtained by the mechanical ball milling during 4 hours. The ball milling was performed by two balanced milling jars with 10 agate balls (diameter 8 mm) in each jar with ethanol as a medium and the speed rate was fixed 600 rpm for successive cycles of 15 minutes.

Table 1. The purity and the manufacturers of raw materials

Reagent	Purity	Manufacturer
ZnO	99.50%	Shanghai Electric Porcelain Works Co., Ltd
MgO	98.50%	Sinopharm Chemical Reagent Co., Ltd
TiO_2	98.00%	Sinopharm Chemical Reagent Co., Ltd
Al_2O_3	99.50%	Sinopharm Chemical Reagent Co., Ltd

Current-voltage (I-V) curves of ZnO ceramic pellets were measured by a self-assembled four-probe digital multimeter composed by a Keithley 6221 current source with 100 mA and a 2182A dual-channel nanovoltmeter. The ZnO particle size of samples **M** and **B** were measured by a Mastersizer 3000 laser particle size analyzer. Scanning electron microscope (SEM) and Transmission electron microscope (TEM) were employed to characterize the particle morphology and the microstructure before and after grinding. To analyze the structural disorder and defects in the samples, the following experiments were employed. X-ray diffraction patterns in the range 2θ=20-70° with a step of 0.013° were obtained by

PANalytical-Empyrean X-ray diffractometer equipped with a Cu-Kα radiation, a pixel detector and a nickel beta filter under 45kV and 30 mA. Raman spectra in the wavenumber range 90-1200 cm^{-1} were collected by a HORIBA Raman X-Plora spectrometer under a ×50 LWD objective microscope with a 532 nm laser diode excitation and an output power of 4 mW. Electron paramagnetic resonance (EPR) experiments were carried out by X-Band (9.5 GHz) Bruker EMX spectrometer. ^{27}Al solid state nuclear magnetic resonance (NMR) experiments were realized on a Bruker Avance III spectrometer at a magnetic field of 7.0 T (corresponding to a ^{1}H Larmor frequency of 300 MHz), equipped with a 2.5 mm VTN dual channel probe.

Results and discussion

The I-V curve of ZnO ceramic sample **C** (Fig. 1a) exhibits a linear characteristic within the measured current range (0-100 mA). The achieved electrical conductivity in bulk ZnO ceramics is as high as 1.52×10^{5} $S\cdot m^{-1}$. A pulse lightning strike experiment was carried out on the **C** sample and the curve of energy density with an impact current is shown in Fig. 1b. The maximum achieved energy density is about 22.42 J/cm^{3} attesting the good electrical properties of the **C** sample.

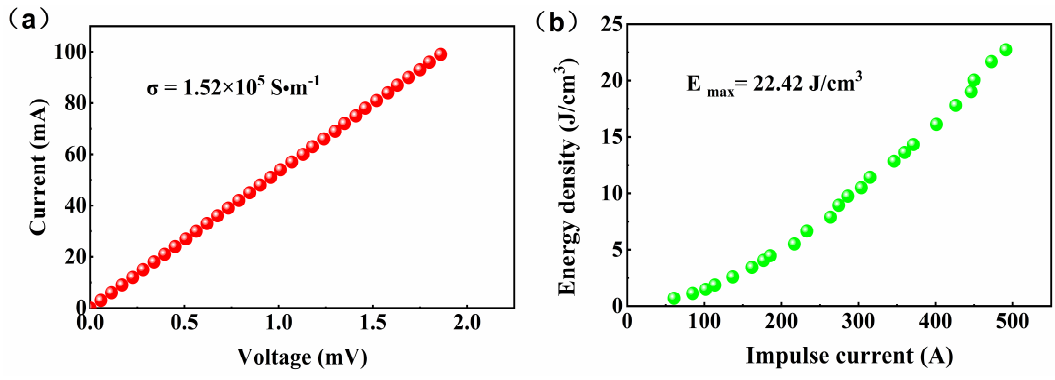

Fig. 1. (a) I-V curve and (b) Energy density vs. impulse current of as-synthesized bulk ZnO ceramics (sample C).

SEM images in Fig. 2 show the microstructures of creamic and particles and the

distributions of the particle sizes of samples **M** and **B**. The schematic microstructures and specific surfaces of the samples are depicted in Fig. 3. For sample **M,** the particle sizes in the range (10-100 µm) are larger than the grain (~10 µm) involved in ZnO ceramics indicating the low grinding efficiency didn't impacts the initial grain structure. Thus, the properties of bulk ZnO ceramics will be coherently obtained on the sample **M**. For the sample **B**, the particle sizes distributed in the range (0.2-2 µm) are smaller than the initial ZnO grains (~10 µm) in ceramics as illustrated by the TEM image in the inset of Fig.2c. The specific surface of sample **B** about 7.63 m^2/g increases drastically compared to the value 1.14 m^2/g obtained in the **M** sample. The resulting samples can reflect the defects concentration and the local order states in finely divided ZnO ceramics. Therefore, the structural properties between ceramics and powder could be indirectly deduced from comparing the properties of samples **M** and **B**.

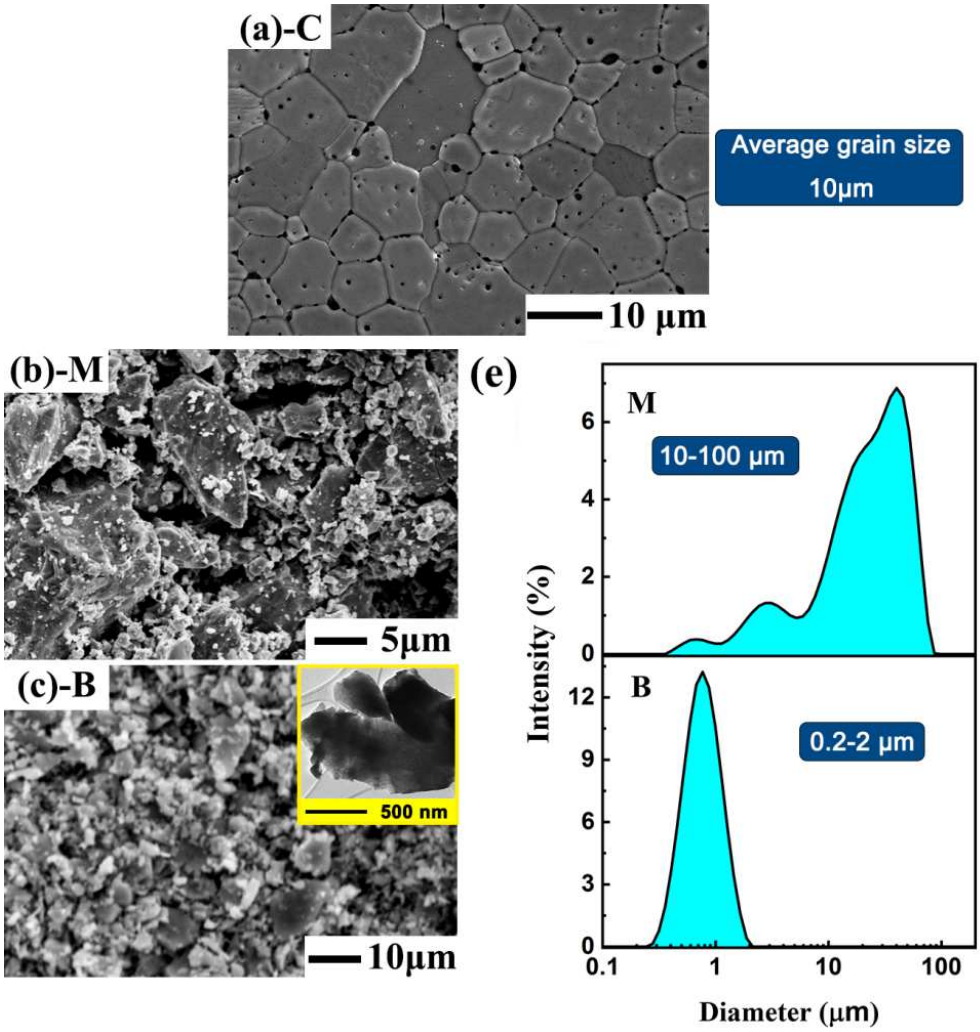

Fig. 2. Average size of ZnO grains and size distribution of samples M and B.The inset in Fig.2c illustrate TEM image of ceramic grains in the B sample.

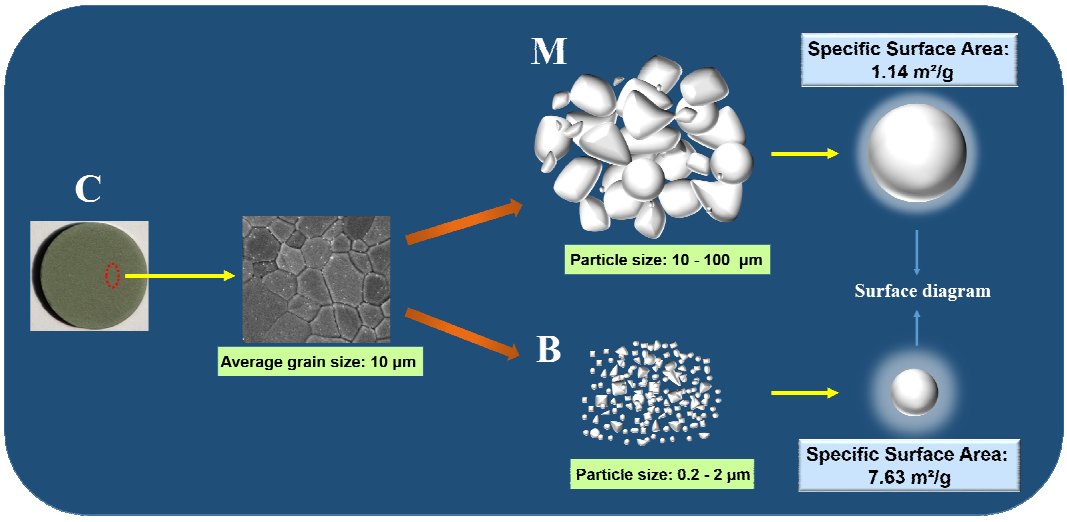

Fig. 3. Schematic diagram of the crushed particles.

XRD patterns reported in Fig. 4 show that the main phase in both samples **M** and **B** is wurtzite ZnO (JCPDS No. 36-1451). For sample **B**, the intensities of all XRD diffraction lines are lowered along with an increase of the full width at half maximum (FWHM) of for (101) line. This behavior is related to low crystalline quality of the **B** sample caused by ball milling. Indeed, the mechanical process contributes to lower the particle sizes and increases the structural disorder at the surface, which can also be traduced from the Raman studies. As shown in Fig. 5, Raman spectra were reported with a normalized intensity of the active Raman modes according to the ZnO characteristic E_2^{high} mode at 443 cm^{-1}. The lineshape of the E_2^{high} mode reflects the local structural disorder, the reduced translational symmetry by defects [17] as well as the reduced particle size. As reported in Fig. 5, the more pronounced band centered at 500 cm^{-1} with a high integrated intensity in sample **M** is assigned to the activation of B_1 mode by the structural disorder. According to our former work [15], Al doping in ZnO contributes to create interstitial Zn ions (Zn_i) which enhance the disorder in the host ZnO lattice. Meanwhile, as the A_1(TO) mode at 382 cm^{-1} is related to oxygen vacancies (V_O) [18], the decrease of its intensity in **B** sample correlates with a low V_O concentration compared to **M** sample. The same behavior is also noticed for the B_1 mode which exhibit lower intensity in the **B** sample. To conciliate coherently the above observations, we suggest that Zn_i and V_O defects are involved partly in the grain boundaries [19]. As the ball milling which reduces the grain size, it limits in fact the concentration of Zn_i and V_O. A further comprehensive analysis is carried out below by using the local probe methods such EPR and NMR experiments.

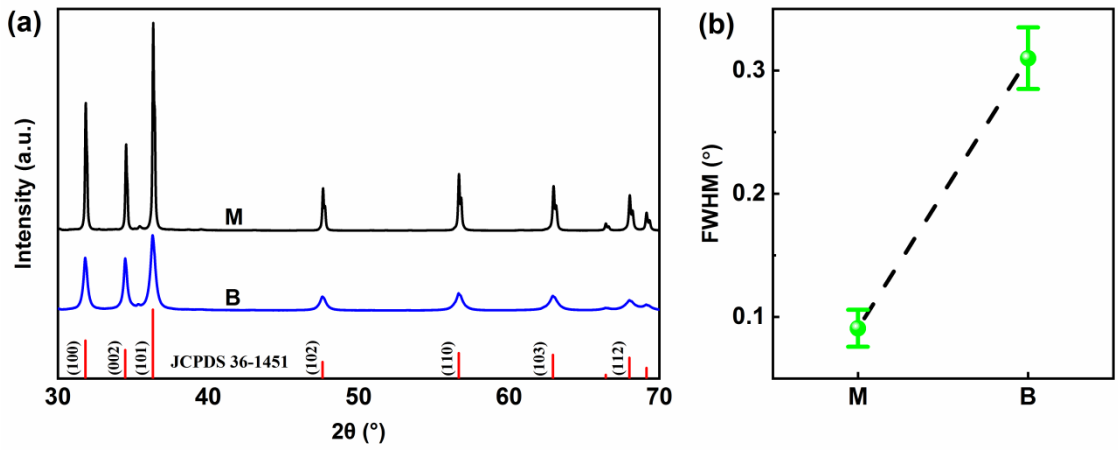

Fig. 4. (a) X-ray diffraction patterns, (b) FWHM of (101) line for samples M and B.

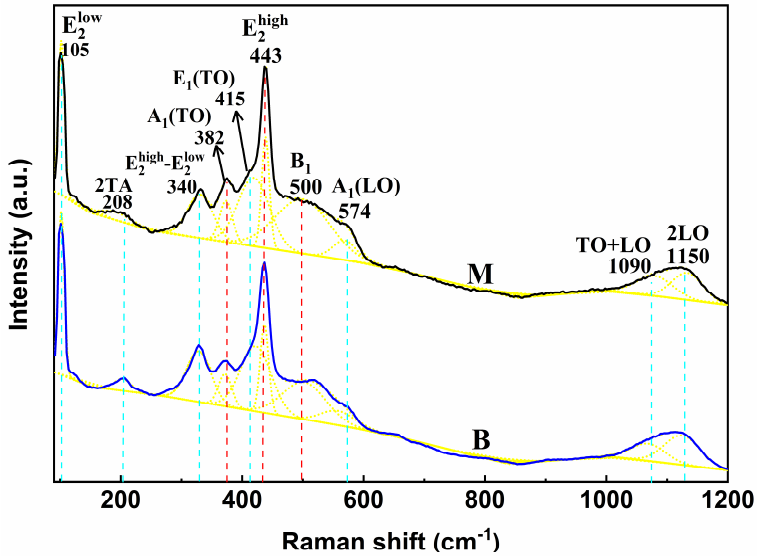

Fig. 5. Raman spectra for samples M and B.

In Fig. 6a, the single resonance line with the g factor at 1.960(2) is a characteristic of an EPR fingerprint of paramagnetic centers involved in ZnO related to Zn_i [15,20]. The Intensity of the EPR signal in the highly conductive sample **M** is quite low in the less conductive sample **B**. In this case, the increased grains boundaries in finely divided powders act as barriers for the conduction channels and then limit the mobility of charge carriers as demonstrated in other families of semiconductors [21]. The occurrence of defects at the grain boundaries is also favored by the high specific surfaces and overcame the charge transport. The thermal evolution of the EPR line width (ΔH) and the integrated line intensity (II_{EPR}) defined as $II_{EPR} \sim I_{EPR} * (\Delta H)^2$ with I_{EPR}

the line intensity are depicted in the range 160K-300 K (Fig. 6b and 6c). In the sample **B**, II_{EPR} follows the well-known Curie law involved for localized and non-interacting paramagnetic centers. This behavior contrasted with that in the **M** sample where a nearly stationary evolution was seen for II_{EPR} versus the temperature. This suggests the existence of Pauli like spin susceptibility induced by delocalized electrons which account for the EPR signal in the **M** sample. Moreover, the EPR linewidth ΔH in the sample **B** remains constant when increasing the temperature while a linear increase is observed for ΔH in sample **M** as it may occur when conduction electrons contribute to the relaxation of the paramagnetic species, according to the so-called Korringa relaxation process. Thus, the thermal behaviors of the spectral parameters of sample **M** is consistent with a high density of conduction electrons leading to the involvement of Pauli spin susceptibility in the integrated line intensity and to the particular relaxation mechanism evidenced by EPR line width. The fact that the sample **M** shows less effective paramagnetic species concentration (Fig. 6c) can be understood by a high mobility and short relaxation times which limit their contribution to the EPR signal. Thus, the intensity of the EPR line may reflects only the localized paramagnetic species in the sample **M**. The low concentration of paramagnetic species in larger sized particles (sample **M**) compared to the smaller one (sample **B**) is coherent with a higher mobility of paramagnetic species in large domains limiting their effective concentration probed by EPR. Thus, the EPR studies of different size samples may inform on the correlation between the paramagnetic species features and the confinement effect which occurs in small sized particles. The decrease in the mobility in particles of sample **B** may be due to the confinement of charges and to the backscattering which occurs on the particle boundaries as outlined in a nanostructured system by Richter and Schmuttenmaer [22]. Therefore, some defects and boundaries in the particle surfaces in the sample **B**, as a scattering region, have an effect to inhibit carrier transport and then lower the conductivity.

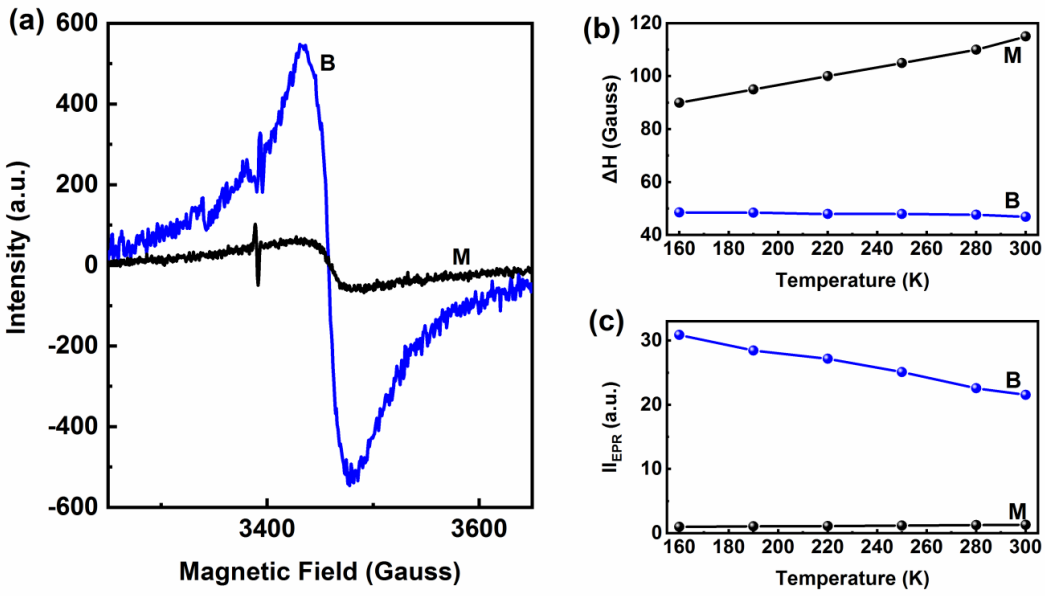

Fig. 6. (a) EPR spectra and thermal evolution of linewidth (ΔH)-(b) and integrated intensity (II_{EPR})-(c) for samples M and B.

To characterize the particle size effects on the NMR signals, we compared the NMR spectra of both samples **M** and **B**. For the environment of ^{27}Al, there are three different coordinated Al in ZnO from the NMR analysis in Fig. 7. The six-coordinated Al (Al^{VI}) is associated to the NMR line at 5 ppm, while the four-coordinated Al (Al^{IV}) give rise to the 80 ppm line. In addition, the NMR line at 185 ppm is accounted by the Knight Shift (KS) effect related to Al_{Zn}-Zn_i complexes [13]. The intensities of NMR lines show different strengths depending on the considered samples **M** and **B**. With the particle size reduction, the NMR line related to Al(KS) decreases drastically while the NMR line for Al^{IV} increases simultaneously; the NMR line for Al^{VI} remains almost the same. Al doping tends to substitute Zn by Al ions in the lattice to form Al_{Zn} in ZnO, while an extended charge delocalization in the high conductive sample occurs from Al_{Zn}-Zn_i complexes, and then induces KS effect [15,23]. Therefore the representative NMR line of Al_{Zn} is marked by the KS effect leading to the 185 ppm line rather than Al^{IV} line at 80 ppm in sample **M**. Besides, in the sample **B**, the low conductivity limits the KS effect and favors the appearance of Al^{IV} line at the chemical shift 80 ppm. A schematic representation of the role of microstructure on the evolution of KS effect may be

drawn as illustrated in Fig. 8. The small sized particles of sample **B**, with higher specific surface area favor the limitation of the extended electronic delocalization around the Al_{Zn}-Zn_i complexes. The density of such Al_{Zn}-Zn_i defect complexes is expected to decease with an increased surface area as in the **B** sample with small particles where a weak Knight Shift effect is manifested on the NMR lines. The Raman, EPR and NMR spectra may be coherently analyzed by considering the Al_{Zn}-Zn_i complexes as the electronic active defects in highly conductive Al doped bulk ZnO materials. Confinement effect and lowering density of the electronic active Al_{Zn}-Zn_i complexes in finely divided sample **B** lower the conductivity and allow a clear evidence of the four coordinated Al in ZnO particles.

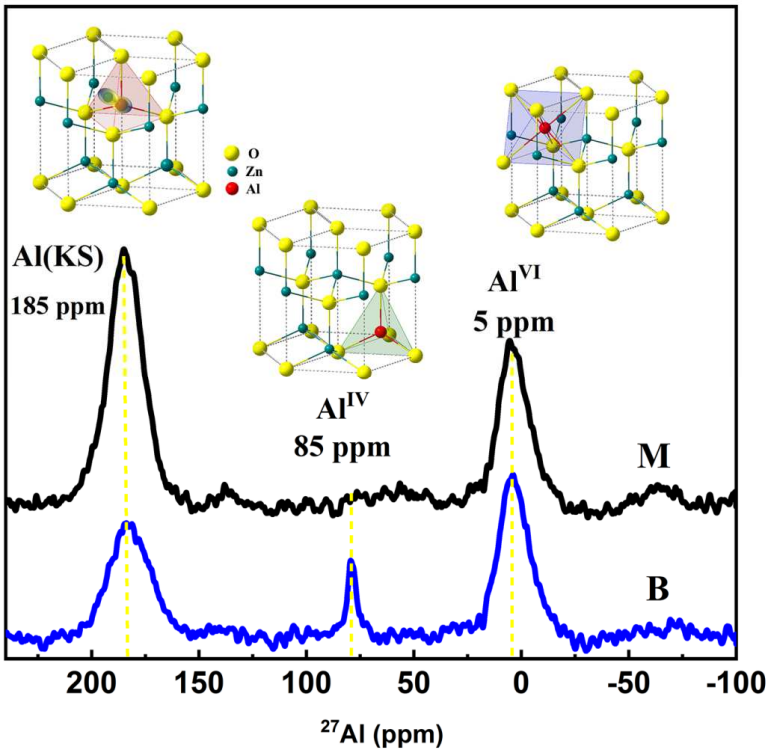

Fig. 7. ^{27}Al MAS NMR spectra of samples M and B.

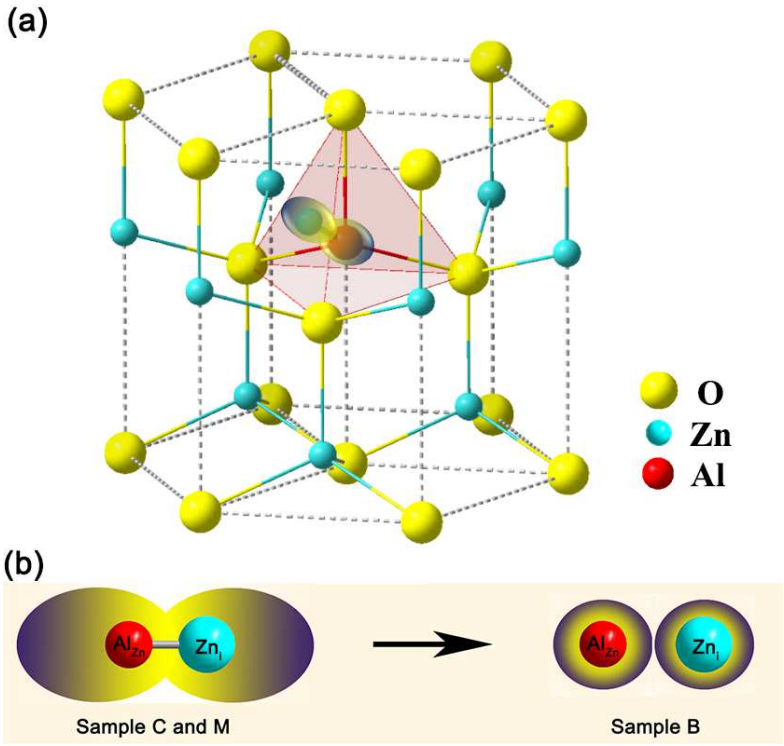

Fig. 8. (a) A crystalline sites with a substitutional Al^{3+}- interstitial Zn^{2+} (Al_{Zn}-Zn_i) in ZnO. (b) Schematic draw of Knight Shift (KS) effect favored for Al_{Zn}-Zn_i complex in bulk C sample and M sample and quite limited KS effect in the B sample with reduced particle sizes.

Conclusion

The role of the microstructure on the local order of Al doping and electronic active defects in Al doped ZnO was analyzed in two different ZnO doped ceramics with different grain sizes. The behavior of the defects such as Al_{Zn}-Zn_i complexes, Al_{Zn} and Zn_i in finely divided ZnO ceramics was compared for particles with different specific surfaces. The local structural disorder is confirmed to be induced by a mechanical ball milling through the broad FWHM in XRD patterns along with broad bands of Al doped ZnO characteristic E_2^{high} mode in Raman spectra. For the electrical behavior of the considered samples, large sized particles favor the formation of Al_{Zn}-Zn_i complexes with extended electronic density leading to a high electrical conductivity up to 10^5 $S{\cdot}m^{-1}$ as it may occurs also in bulk Al doped ZnO ceramics . In this issue, the Knight

shift effect induced in highly conductive sample **M** leads to a particular NMR line at 185 ppm far from any known oxygen coordinated ^{27}Al. The formation of small particles by a ball milling (sample **B**) overcame the stability of Al_{Zn}-Zn_i complexes and the effect of the microstructure which confine the charge carriers. This fact limits the conductivity and the KS effect leading to a resolved NMR line associated to four oxygen coordinated ^{27}Al. In parallel, the involved defects structures were pointed out by EPR spectroscopy as the function of ZnO grain sizes. The EPR signal assigned to Zn_i defects is characterized by different line intensities and widths depending on the microstructures features. The easy delocalization of charge carriers in larger size particles limits their contribution to the EPR signal. Oppositely, the less conductive sample **B** shows a higher concentration of paramagnetic centres due to less effects from the conduction electrons on the relaxation mechanisms which alters the EPR line width. The performed experiments dealing with the structural and local order analysis of the doping element coordinations and electronic defects contribute to consistent analysis of the correlation between the microstructure and the electrical behavior in Al doped ZnO structures.

Acknowledgments

Projects supported by the National Key R&D Program of China (No. 2016YFA0201103, 2016YFB0402701), the National Basic Research Program of China under Grant (No. 2015CB654605), National Nature Science Foundation of China (No. 51831010, 51672293, 51807195) and the Instrument Developing Project of Chinese Academy of Sciences (No. ZDKYYQ20180004). We acknowledge the support from the project PHC CAI YUANPEI number N°41475SH. Q. Sun would like to thank to Campus France for the Excellence Eiffel Grant (2017-2018) at Le Mans University and to the Polish National Agency for the program PROM at Jan Dlugosz University in Czestochowa (Poland).

Reference

[1] C. Pan, J. Zhai, Z. Wang. Piezotronics and Piezo-phototronics of Third Generation Semiconductor Nanowires. Chem. Rev. 119 (2019) 9303-59.

[2] A. Janotti, C. Van de Walle. Fundamentals of zinc oxide as a semiconductor. Rep. Prog. Phys. 72 (2009) 126501 .

[3] J. Zhang, T. Tan, Y. Zhao, N. Liu. Preparation of ZnO Nanorods/Graphene Composite Anodes for High-Performance Lithium-Ion Batteries. Nanomaterials-basel. 8 (2018) 966.

[4] S. Ghosh, A. Mallick, B. Dou, M. F. A. M. van Hest, S. Garner, D. Basak. A novel blanket annealing process to achieve highly transparent and conducting Al doped ZnO thin films: Its mechanism and application in perovskite solar cells. Sol. Energy. 174 (2018) 815-25.

[5] K. Kato, H. Qiu, E. Khutoryan, Y. Tatematsu, M. Tani, T. Idehara, et al. Strong yellow emission of high-conductivity bulk ZnO single crystals irradiated with high-power gyrotron beam. Appl. Phys. Lett. 111 (2017) 031108.

[6] P. Meng, J. Wu, X. Yang, J. Hu, J. He. Electrical properties of ZnO varistor ceramics modified by rare earth-yttrium and gallium dopants. Mater. Lett. 233 (2018) 20-3.

[7] A. Ghosh, C. Zhang, S. Shi, H. Zhang. High temperature CO_2 sensing and its cross-sensitivity towards H2 and CO gas using calcium doped ZnO thin film coated langasite SAW sensor. Sensor. Actuat. B-Chem. 301 (2019) 126958.

[8] T. Tian, L. Cheng, L. Zheng, J. Xing, H. Gu, S. Bernik, et al. Defect engineering for a markedly increased electrical conductivity and power factor in doped ZnO ceramic. Acta. Mater. 119 (2016) 36-44.

[9] Z. Yan, J. Bao, X. Yue, X. Li, Y. Zhou, X. Wu. Impacts of preparation conditions on photoelectric properties of the ZnO:Ge transparent conductive thin films fabricated by pulsed laser deposition. J. Alloy. Compd. 812 (2020) 152093.

[10] S. Liu, J. Liu, W. Jiang, C. Liu, W. Ding, H. Wang, et al. Aluminum- and

boron-co-doped ZnO ceramics: structural, morphological and electrical characterization. Appl. Phys. A-Mater. 122 (2016) 878.

[11] X. Liang. Thermoelectric transport properties of naturally nanostructured Ga–ZnO ceramics: Effect of point defect and interfaces. J. Eur. Ceram. Soc. 36 (2016) 1643-50.

[12] M. A. Awad, A. M. Ahmed, V. O. Khavrus, E. M. M. Ibrahim. Tuning the morphology of ZnO nanostructure by in doping and the associated variation in electrical and optical properties. Ceram. Int. 41 (2015) 10116-24.

[13] A. Momot, M. Amini, G. Reekmans, D. Lamoen, B. Partoens, D. Slocombe, et al. A novel explanation for the increased conductivity in annealed Al-doped ZnO: an insight into migration of aluminum and displacement of zinc. Phys. Chem. Chem. Phys. 19 (2017) 27866-77.

[14] Q. Sun, G. Li, T. Tian, J. Zeng, K. Zhao, L. Zheng, et al. Co□doping effects of (Al, Ti, Mg) on the microstructure and electrical behavior of ZnO based ceramics. J. Am. Ceram. Soc. 103 (2020) 3194–3204.

[15] Q. Sun, T. Tian, L. Zheng, Z. Man, G. Li, M. Barré, et al. Electronic active defects and local order in doped ZnO ceramics inferred from EPR and ^{27}Al NMR investigations. J. Eur. Ceram. Soc. 39 (2019) 3070-6.

[16] Q. Sun, G. Li, T. Tian, Z. Man, L. Zheng, M. Barré, et al. Controllable microstructure tailoring for regulating conductivity in Al-doped ZnO ceramics. J. Eur. Ceram. Soc. 40 (2020) 349-54.

[17] T. Tian, L. Zheng, X. Ruan, G. Li. Disorder-induced localization in doped ZnO by different sintering atmosphere. Ceram. Int. 44 (2018) S195-S198.

[18] S. Olive-Méndez, C. Santillán-Rodríguez, R. González-Valenzuela, F. Espinosa-Magaña, J. Matutes-Aquino. Role of vanadium ions, oxygen vacancies, and interstitial zinc in room temperature ferromagnetism on ZnO-V_2O_5 nanoparticles. Nanoscale. Res. Lett. 9 (2014) 169.

[19] Raphael Lucas de Sousa e Silva, A. Franco. Effect of porosity on dielectric properties of ZnO ceramics. J. Eur. Ceram. Soc. 40 (2020) 1307-11.

[20] S. Hartner, M. Ali, C. Schulz, M. Winterer, H. Wiggers. Electrical properties of aluminum-doped zinc oxide (AZO) nanoparticles synthesized by chemical vapor synthesis. Nanotechnology. 20 (2009) 445701.

[21] B. Alberding, A. Biacchi, A. Hight Walker, E. Heilweil. Charge Carrier Dynamics and Mobility Determined by Time-Resolved Terahertz Spectroscopy on Films of Nano-to-Micrometer-Sized Colloidal Tin(II) Monosulfide. J. Phys. Chem. C. 120 (2016) 15395-406.

[22] C. Richter, C. Schmuttenmaer. Exciton-like trap states limit electron mobility in TiO_2 nanotubes. Nat. Nanotechnol. 5 (2010) 769-72.

[23] K. Cai, E. Müller, C. Drašar, A. Mrotzek. Preparation and thermoelectric properties of Al-doped ZnO ceramics. Mater. Sci. Eng. B-Adv. 104 (2003) 45-8.